PAPER

Technological exploitation of the JET neutron environment: progress in ITER materials irradiation and nuclear analysis

To cite this article: L.W. Packer *et al* 2021 *Nucl. Fusion* **61** 116057

IOP Publishing | International Atomic Energy Agency Nuclear Fusion

Nucl. Fusion **61** (2021) 116057 (16pp) https://doi.org/10.1088/1741-4326/ac2a6b

Technological exploitation of the JET neutron environment: progress in ITER materials irradiation and nuclear analysis

L.W. Packer[1,*], P. Batistoni[2], N. Bekris[3], S.C. Bradnam[1], M. Fabbri[4], Z. Ghani[1], M.R. Gilbert[1], R. Kierepko[5], E. Łaszyńska[6], D. Leichtle[3], I. Lengar[7], S. Loreti[2], J.W. Mietelski[5], C.R. Nobs[1], M. Pillon[2], M.I. Savva[8], I.E. Stamatelatos[8], T. Vasilopoulou[8], A. Wójcik-Gargula[5], A. Zohar[7] and JET Contributors[a]

[1] CCFE, United Kingdom Atomic Energy Authority, Culham Science Centre, Abingdon, Oxon, OX14 3DB,
United Kingdom
[2] ENEA-Department of Fusion and Technology for Nuclear Safety and Security, via E. Fermi 45, 00044 Frascati (Rome), Italy
[3] Karlsruhe Institute of Technology (KIT), Hermann-von-Helmholtz Platz 1, 76344 Eggenstein-Leopoldshafen, Germany
[4] Fusion for Energy, Josep Pla 2, Torres Diagonal Litoral B3, 08019 Barcelona, Spain
[5] Institute of Nuclear Physics, Polish Academy of Sciences, PL-31-342 Krakow, Poland
[6] Institute of Plasma Physics and Laser Microfusion, 01-497 Warsaw, Poland
[7] Reactor Physics Department, Jožef Stefan Institute, Jamova cesta 39, SI-1000 Ljubljana, Slovenia
[8] Institute of Nuclear and Radiological Sciences, Technology, Energy and Safety, NCSR Demokritos, Athens, 15310, Greece

E-mail: lee.packer@ukaea.uk

Received 18 May 2021, revised 16 September 2021
Accepted for publication 27 September 2021
Published 14 October 2021

Abstract

Several experimental activities have been conducted within the 'ACT' sub-project under the EUROfusion WPJET3 programme with the purpose to ultimately irradiate ITER materials within the JET D–T neutron environment. The latest results of these activities are presented in this work. The ITER materials include: poloidal field coil jacket samples and toroidal field coil radial closure plate steels, EUROFER 97-2 steel, W and CuCrZr materials from the divertor, Inconel 718, CuCrZr and 316L stainless steel for blanket modules and vacuum vessel forging samples. The experimental results presented here include gamma spectrometry measurements and analysis obtained from post-irradiated samples following the 2019 C38 (D–D) campaign, where a total of 97 samples were irradiated in a newly prepared long-term irradiation station assembly, comprising 27 ITER material samples, 70 dosimetry foils and two combination-foil detectors, known as 'VERDI' detectors. Measurements using a range of dosimetry reactions that are present in the IRDFF-II nuclear data file have also been used in preparatory work to characterise the irradiation locations. The latest ITER sample measurement results are presented along with initial comparisons with corresponding neutron transport and activation calculation predictions.

Keywords: neutronics, activation, JET, ITER

(Some figures may appear in colour only in the online journal)

* Author to whom any correspondence should be addressed.
[a] See Joffrin *et al* 2019 (https://doi.org/10.1088/1741-4326/ab2276) for the JET Contributors.

1. Introduction

Understanding the effects of neutron irradiation impact on materials is one of the outstanding issues in the development of fusion technologies. There is an imminent opportunity to learn from material exposure within the Joint European Torus (JET) tokamak environment during deuterium–tritium (D–T) operations, to gather data and take advantage of the significant 14 MeV neutron fluence to irradiate samples that will be used in the manufacturing of main ITER tokamak components. The impact of this work derives from the opportunity, for the first time in a tokamak operating with a D–T plasma, to deliver experimental results which inform on the nuclear characteristics of samples of ITER structural materials (and importantly their inherent impurities) exposed to neutrons. The experiments planned to commence in 2021/22 at JET, notably including T–T and D–T experimental phases, are expected to produce significant neutron yields, in the region of 10^{21} neutrons. Whilst the JET integrated D–T neutron yield is significant it is important to put this integrated yield into the context of the much higher neutron yield expected at the ITER device during the 500 MW D–T fusion power phase, which will emit 1.77×10^{20} neutrons per second from the plasma with an expected integrated yield, based on 4700 h operation at 500 MW, of 10^{27} neutrons. The experimental work to date at JET has therefore focussed primarily on neutron activation and residual radiation fields rather than material degradation phenomena in fusion neutron fields. However, future activities, following D–T operations at JET, will aim to measure some materials damage phenomena in post-irradiated samples using sensitive positron annihilation lifetime spectroscopy (PALS) techniques. The scientific objectives are linked with an EUROfusion nuclear technology programme, WPJET3, to deliver the maximum scientific and technological return from JET operations. The associated experimental data from D–D, T–T and D–T operations are providing, and will provide in the future, new data to develop and improve the radiation transport and activation simulation capabilities via benchmarking and validation studies in fusion tokamak relevant operational conditions. Significant results have been obtained to date with a focus on relevance to ITER device operations [1]. The nuclear activities that have been performed include the 14 MeV calibration of neutron yield monitors [2], neutronics benchmark experiments [3–7], nuclear diagnostics and data processing for tritium breeding blankets [8], and activation measurements with supporting analyses for fusion materials [9–11].

The experimental results presented in this paper include gamma spectrometry measurements and analysis obtained as part of the JET 2019 C38 deuterium campaign, where samples were irradiated over a period of 147 d in a newly prepared long-term irradiation station (LTIS) assembly (see figure 1) in a location very close to the JET vacuum vessel, outside of the vacuum boundary. The samples were extracted following their irradiation and then distributed to a number of EU laboratories for gamma spectrometry analysis, to identify the nuclides present and to accurately determine their activity. The latest measurement results are presented in this paper and are compared with corresponding calculations using the FISPACT-II inventory code [12, 13] with ITER material compositions linked with neutron spectra derived from recent MCNP radiation transport calculations [14] performed using a detailed JET model containing the LTIS, material sample geometry and material compositions.

2. The long-term irradiation station and sample loading configuration

Our extensive earlier work showing the characterisation of two previously used LTIS assemblies (used in the C36 JET D–D campaign) is detailed in [11]. Since then a new LTIS has been designed to position samples of materials to be irradiated close to the JET vessel wall, but remaining outside of the JET vacuum boundary. This ensures that samples will experience a relatively high neutron fluence (compared to being located at a further radial distance from the plasma source of neutrons) during their irradiation while enabling convenient retrieval management without breach of the vacuum boundary. The assembly was loaded with ITER material and dosimetry foil samples via an 'ACT' assembly holder machined from 316L steel, which comprises 26 sample cavity positions. For the ACT holder each cavity is 3 mm depth and can accommodate samples up to 18 mm diameter. The dosimetry foils provide a measurement of the absolute neutron fluence at the LTIS and they have been used to verify the calculation of neutron fluence at the samples using the measured neutron yield. Figure 1 shows an image of the assembly following loading into octant 7 within JET and shows the numbering scheme associated with the 26 positions. 27 ITER material samples were loaded into the ACT cassette with 20 unique materials from different manufacturers. The new LTIS is also designed to enable the irradiation of functional materials with high neutron fluence via an adjacent (to the ACT holder) sample holder, referred to as the 'RADA' holder, as part of a related WPJET3 project.

3. ITER material sample details

3.1. Sample preparation activities

A range of real ITER materials from different manufacturers and used for different ITER components were sourced by Fusion for Energy (F4E). The materials, related identifiers and sources are detailed in table 1. The materials were accompanied by elemental composition analysis certificates. These bulk materials, in various different forms, were shipped to CCFE and were then cut and machined by UKAEA's Special Techniques Group to form disc samples that were also uniquely etched (labelled) using a punching technique. The ITER sample dimensions are specified in the table.

3.2. ITER material elemental compositions

Elemental material descriptions from the corresponding certificates that were provided are detailed by mass fraction in

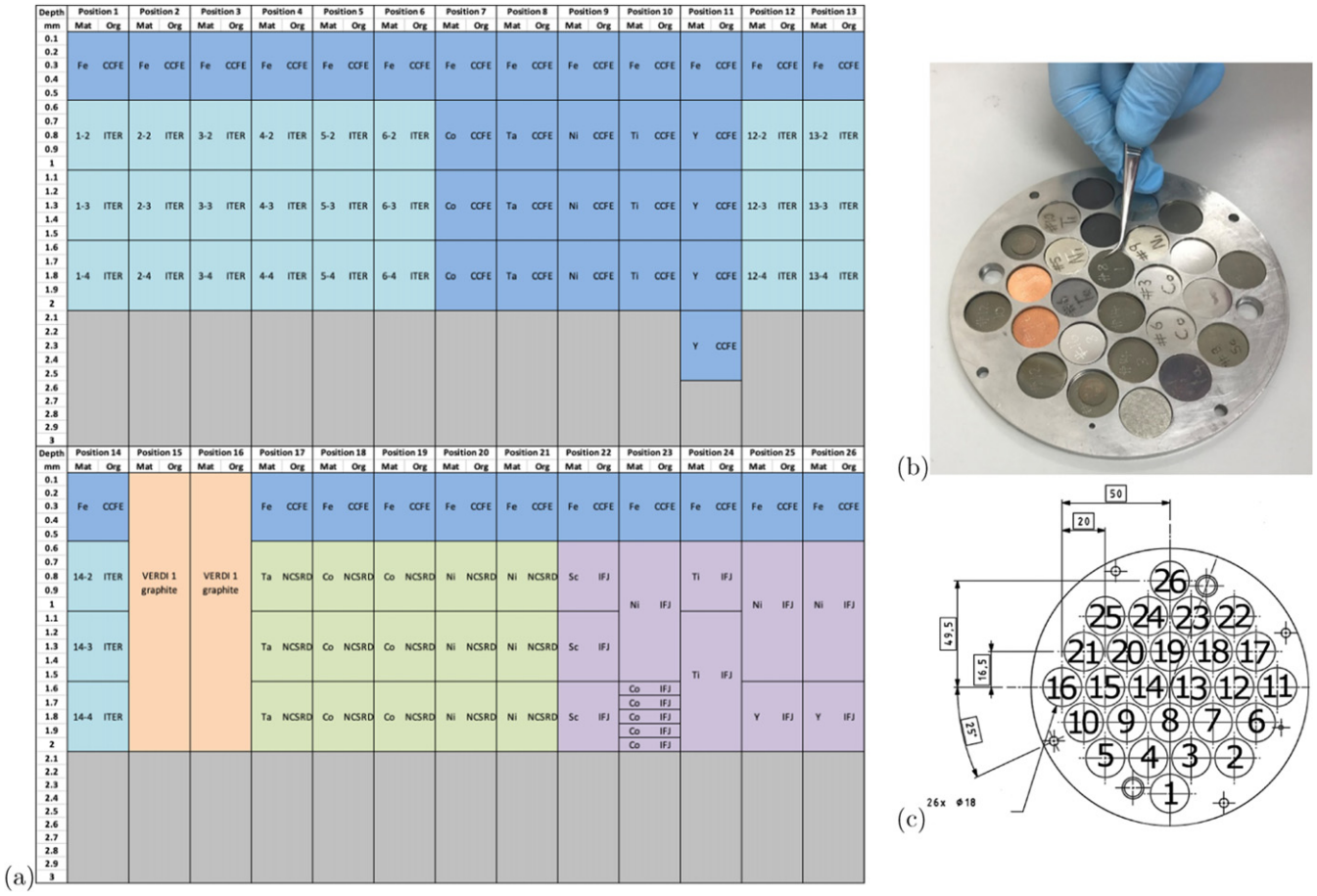

Figure 1. (*a*) LTIS dosimetry foil and ITER material sample arrangement for the C38 experimental campaign by position number (1–26) in columns, and by approximate cavity depth (up to 3 mm) in rows. For reference, samples at 0.1–0.5 mm depth are closer to the plasma (see e.g. figure 4 in [15]), with the distance to the plasma increasing by increased depth. The position numbers indicated in (*a*) correspond to those shown in the physically representative drawing in (*c*), which also indicates the key dimensions in mm. In (*a*) the ITER materials are shown as light blue boxes with a corresponding unique position–depth identifier, which may be matched with table 1 to provide the full ITER material description which can be uniquely mapped to this figure. Other colours shown in (*a*) denote the institute laboratory responsible for post-irradiation analysis of various dosimetry foils: dark blue-CCFE; green and orange-NCSRD; purple IFJ/IPPLM. The photo in (*b*) is the LTIS assembly holder loaded with these samples.

table 2. They include samples from the poloidal field coil jacket and toroidal field coil radial closure plate steels, EUROFER 97-2 steel, W and CuCrZr materials from the divertor, Inconel 718, CuCrZr and 316L stainless steel for blanket modules and vacuum vessel forging samples. EUROFER 97-2 steel (Fe-9Cr-1W-0.2V-0.12Ta) is planned to be tested within the ITER test blanket modules and is a reduced activation ferritic/martensitic (RAFM) steel. RAFM steels are the benchmark structural material for in-vessel components of fusion reactors such as DEMO. These material compositions have been used as input to the series of inventory simulation output results provided in section 5.

Whilst the complete data sets are listed in the table, selected different steel alloys are also compared graphically in the histogram plots in figure 2(a) which gives an indication of the variation in elemental compositions from different steel types and also provides a direct comparison of the family of 316L steel alloy compositions in figure 2(b). Figure 2(c) shows the elemental composition for relevant materials as defined in the ITER materials activation handbook [16] and from [17].

4. Sample retrieval and gamma spectrometry measurements

The LTIS assembly containing the samples was retrieved on 3rd January 2020, approximately 13 d following the end of irradiation. The contact gamma dose rate on this date from the bulk LTIS assembly, (predominantly due to the steel in the assembly cassette which is approximately 2.3 kg) was measured by the CCFE Health Physics group to be 65 μSv h^{-1}. The samples were then extracted from the cassette in CCFE's radiometric laboratory and some of the samples were then shipped for high resolution gamma spectrometry measurements at a number of European laboratories: ENEA, IFJ-PAN, IPPLM, NCSRD as well as some being analysed at CCFE. The ITER samples were distributed according to the laboratories responsible for analysis indicated in table 1. Each laboratory reported results which included the measured sample

Table 1. ITER material description, unique LTIS position ID and other relevant details for irradiated samples exposed during the JET C38 irradiation campaign. The sample LTIS position–depth ID may be used to map to the LTIS configuration shown in figure 1. Nominal dimension are provided as an indication but only the sample mass was measured.

Sample LTIS position–depth ID	Material	Manufacturer and sample details	Analysis laboratory	Sample batch ID	Measured sample mass (g)	Nominal thickness (mm)	Nominal diameter (mm)	Nominal density (g cm^{-3})
1-2	EUROFER 97-2	Saarschmiede Gmbh vacuum induction melting (VIM) + vacuum arc remelting (VAR) 1.4914 × 3 EUROFER 97-2, order No. 8186097	CCFE (UK)	6a_8	0.356	0.5	11	7.87
3-2	Al–Bronze	Aubert & Duval, used for the ITER inner vertical target (IVT), Copper Alloys Ltd. cast ID: 51519051		9_2	0.857	0.5	17.5	7.6
5-3	Tungsten	AT & M for ATMOSTAT, W monoblocks, purity 99.5, ref: PD-13482-999		13_1	0.705	0.5	10	19.3
5-2	A660 alloy	Carpenter powder products, India DA, ITER in wall shield (IWS), heat Nr 5600413		10a_10	0.886	0.5	17.5	7.92
6-4	316L(N)	Thyssen Krupp materials France SAS, radial plates for the ITER toroidal field coils, 316LN class C2 solution treated and quenched, stress relieved (2500/33)		4*c*_9	0.506	0.5	13	7.93
12-4	316L(N)	Special TF cover plate (304757)		3a_1	0.927	0.5	17.5	7.93
12-3	XM19	Aubert & Duval, forgings for divertor cassette		14_3	0.921	0.5	17.5	7.88
12-2	316L	Salzgitter Mannesmann Stainless Tubes GmbH, poloidal field coil jacket		2_10	0.886	0.5	17.5	7.93
14-3	Inconel	Inconel alloy 718		8_1	0.967	0.5	17.5	8.2
14-2	316L	Divertor Nadege 316L		15_3	0.92	0.5	17.5	7.93
3-4	316L(N)-IG	Thyssen Krupp Materials France SAS, forged block ITER grade vacuum vessel plate, specimen number 5939		5b_1	0.925	0.5	17.5	7.93
3-3	CuCrZr	Yamato, first wall component, divertor pipe 212601		11b_4	0.953	0.5	17.5	8.9
2-3	A660 alloy	ITER divertor material		12_1	0.925	0.5	17.5	7.92

Table 1. (Continued)

Sample LTIS position–depth ID	Material	Manufacturer and sample details	Analysis laboratory	Sample batch ID	Measured sample mass (g)	Nominal thickness (mm)	Nominal diameter (mm)	Nominal density (g cm^{-3})
1-4	316L(N)-IG	Industeel Groupe Arcelor, ITER vacuum vessel plate	ENEA (Italy)	5a_9	0.9258	0.5	17.5	7.93
4-4	316L(N)	Thyssen Krupp Materials France SAS, radial plates (jacket) for the ITER toroidal field coils (2500/64)		4a_9	0.8795	0.5	17.5	7.93
14-4	316L(N)	Special TF cover plate (304756)		3*c*_1	0.9258	0.5	17.5	7.93
1-3	A660 alloy	ITER divertor material		12_10	0.924	0.5	17.5	7.92
6-3	Tungsten	AT & M for ATMOSTAT, W monoblocks, purity 99.5, ref: PD-13482-999		13_10	0.756	0.5	10	19.3
13-3	XM-19	Aubert & Duval, forgings for the ITER divertor cassette		14_1	0.9104	0.5	17.5	7.88
2-2	EUROFER 97-2	Saarschmiede GmbH, vacuum induction melting (VIM) + vacuum arc remelting (VAR) 1.4914 × 3, EUROFER 97-2, order no: 8186097		6b_1	0.5023	0.5	11	7.87
6-2	SS304	Carpenter Powder Products, India DA, in wall shield sample (IWS)		10b_2	0.9236	0.5	17.5	7.85
13-2	A286 alloy	Villares Metals, ITER in wall shield (IWS)	IFJ/IPPLM (Poland)	7_1	0.9172	0.5	17.5	7.92
4-3	CuCrZr	KME, first wall component, divertor pipe 212606		11a_1	1.0018	0.5	17.5	7.93
13-4	316L(N)	Special TF cover plate (304761)		3b_1	0.9381	0.5	17.5	7.93
4-2	Al-bronze	Aubert & Duval Copper alloys Ltd. For the inner vertical target (IVT), cast ID: 51519051	NCSRD (Greece)	9_3	0.85251	0.5	17.5	7.45
5-4	316L(N)	Thyssen Krupp Materials France SAS, radial plates for the ITER toroidal field coils, 316LN class C2 solution treated and quenched, stress relieved (2500/68)		4b_10	0.88502	0.5	17.5	7.93
2-4	316L(N)-IG	R Kind GmBh, ITER vacuum vessel plate		5c_9	0.92449	0.5	17.5	7.93

Table 2. ITER material elemental compositions defined by the provided material certificates. Samples may be linked to the sample description provided in table 1 by their LTIS position–depth ID. Values provided are weight fractions. Where mass ranges have been specified in the certificate, the maximum value has been listed.

	Material type; LTIS position–depth ID									
Element	EUROFER 97-2; 1-2, 2-2	SS316L; 12-2	XM19; 12-3, 13-3	SS316L(N); 12-4	A286; 13-2	SS316L(N); 13-4	316L; 14-2	Inconel; 14-3	SS316L(N); 14-4	SS316L(N)-IG; 1-4
B	2.000×10^{-5}	—	—	6.000×10^{-6}	5.900×10^{-5}	6.000×10^{-6}	—	6.000×10^{-5}	1.200×10^{-5}	2.000×10^{-5}
C	1.200×10^{-3}	3.000×10^{-4}	6.000×10^{-4}	2.200×10^{-4}	3.800×10^{-4}	2.200×10^{-4}	6.000×10^{-4}	8.000×10^{-4}	2.200×10^{-4}	3.000×10^{-4}
N	4.500×10^{-4}	—	4.000×10^{-3}	1.850×10^{-3}	—	—	4.000×10^{-3}	—	1.850×10^{-3}	8.000×10^{-4}
O	1.000×10^{-4}	—	—	—	—	—	—	—	—	—
Al	1.000×10^{-4}	—	—	—	3.100×10^{-3}	—	—	8.000×10^{-3}	—	—
Si	5.000×10^{-4}	7.500×10^{-3}	1.000×10^{-2}	3.000×10^{-3}	6.200×10^{-3}	3.200×10^{-3}	1.000×10^{-2}	3.500×10^{-3}	3.400×10^{-3}	5.000×10^{-3}
P	5.000×10^{-5}	3.000×10^{-4}	4.000×10^{-4}	1.800×10^{-4}	1.400×10^{-4}	1.800×10^{-4}	4.000×10^{-4}	1.500×10^{-4}	1.700×10^{-4}	2.500×10^{-4}
S	5.000×10^{-5}	1.000×10^{-4}	3.000×10^{-4}	1.000×10^{-5}	1.100×10^{-5}	1.000×10^{-5}	3.000×10^{-4}	1.500×10^{-4}	1.000×10^{-5}	—
Ti	2.000×10^{-4}	—	—	—	2.260×10^{-2}	—	—	1.150×10^{-2}	—	1.500×10^{-4}
V	2.500×10^{-3}	—	3.000×10^{-3}	—	2.700×10^{-3}	—	3.000×10^{-3}	—	—	—
Cr	9.500×10^{-2}	1.850×10^{-1}	2.350×10^{-1}	1.819×10^{-1}	1.510×10^{-1}	1.817×10^{-1}	2.350×10^{-1}	2.100×10^{-1}	1.819×10^{-1}	1.800×10^{-1}
Mn	6.000×10^{-3}	2.000×10^{-2}	6.000×10^{-2}	1.150×10^{-2}	1.500×10^{-2}	1.150×10^{-2}	6.000×10^{-2}	3.500×10^{-3}	1.160×10^{-2}	2.000×10^{-3}
Fe	8.794×10^{-1}	6.208×10^{-1}	5.181×10^{-1}	6.527×10^{-1}	5.277×10^{-1}	6.532×10^{-1}	5.181×10^{-1}	1.188×10^{-1}	6.534×10^{-1}	6.806×10^{-1}
Co	1.000×10^{-4}	1.000×10^{-3}	5.000×10^{-4}	3.000×10^{-4}	4.000×10^{-4}	5.000×10^{-5}	5.000×10^{-4}	2.000×10^{-3}	3.000×10^{-4}	2.500×10^{-3}
Ni	1.000×10^{-4}	1.400×10^{-1}	1.350×10^{-1}	1.231×10^{-1}	2.580×10^{-1}	1.229×10^{-1}	1.350×10^{-1}	5.500×10^{-1}	1.215×10^{-1}	1.250×10^{-1}
Cu	1.000×10^{-4}	—	—	—	3.000×10^{-4}	—	—	3.000×10^{-3}	—	4.000×10^{-4}
Zn	1.250×10^{-4}	—	—	—	—	—	—	—	—	—
As	1.250×10^{-4}	—	—	—	—	—	—	—	—	—
Zr	1.250×10^{-4}	—	—	—	—	—	—	—	—	—
Nb	5.000×10^{-5}	—	3.000×10^{-3}	—	—	—	3.000×10^{-3}	5.500×10^{-2}	—	1.000×10^{-4}
Mo	5.000×10^{-5}	2.500×10^{-2}	3.000×10^{-2}	2.520×10^{-2}	1.240×10^{-2}	2.520×10^{-2}	3.000×10^{-2}	3.300×10^{-2}	2.560×10^{-2}	2.700×10^{-3}
Cd	—	—	—	—	—	—	—	—	—	—
Sn	—	—	—	—	—	—	—	—	—	—
Sb	1.250×10^{-4}	—	—	—	—	—	—	—	—	—
Ta	1.400×10^{-3}	—	1.000×10^{-4}	—	—	—	1.000×10^{-4}	5.000×10^{-4}	—	1.000×10^{-4}
W	1.200×10^{-2}	—	—	—	—	—	—	—	—	—
Pb	—	—	—	—	1.000×10^{-6}	—	—	—	—	—

	A660; 2-3 1-3	**SS316L(N)-IG; 2-4**	**SS316L(N)-IG; 3-4**	**Al-bronze; 4-2**	**CuCrZr; 4-3 3-3**	**SS316L(N); 4-4**	**A660; 5-2**	**Tungsten; 5-3, 6-3**	**SS316L(N); 5-4**	**SS304; 6-2**
B	1.000×10^{-4}	1.400×10^{-5}	6.000×10^{-6}	—	—	2.000×10^{-5}	5.500×10^{-5}	—	2.000×10^{-5}	—
C	8.000×10^{-4}	1.400×10^{-4}	1.600×10^{-4}	—	—	3.000×10^{-4}	3.800×10^{-4}	3.000×10^{-6}	3.000×10^{-4}	4.300×10^{-4}
N	—	7.000×10^{-4}	7.300×10^{-4}	—	—	2.200×10^{-3}	—	3.800×10^{-5}	2.200×10^{-3}	8.800×10^{-4}
O	—	—	—	—	—	—	—	1.000×10^{-4}	—	—
Al	3.500×10^{-3}	—	2.600×10^{-4}	8.730×10^{-2}	—	—	3.100×10^{-3}	—	—	—
Si	1.000×10^{-2}	3.100×10^{-3}	2.400×10^{-3}	1.000×10^{-4}	—	5.000×10^{-3}	6.200×10^{-3}	1.000×10^{-4}	5.000×10^{-3}	4.200×10^{-3}
P	4.000×10^{-4}	2.200×10^{-4}	1.900×10^{-4}	—	—	2.000×10^{-4}	1.400×10^{-4}	—	2.000×10^{-4}	3.800×10^{-4}
S	3.000×10^{-4}	5.000×10^{-5}	5.000×10^{-5}	—	—	1.500×10^{-4}	1.000×10^{-5}	—	—	2.000×10^{-4}
Ti	2.350×10^{-2}	6.000×10^{-5}	2.600×10^{-5}	—	—	—	2.260×10^{-2}	—	—	—
V	5.000×10^{-3}	—	3.800×10^{-3}	—	—	—	2.700×10^{-3}	—	—	—
Cr	1.600×10^{-1}	1.716×10^{-1}	1.756×10^{-1}	—	9.000×10^{-3}	1.850×10^{-1}	1.510×10^{-1}	—	1.850×10^{-1}	1.845×10^{-1}

Table 2. (Continued)

Element	Material type; LTIS position–depth ID									
	EUROFER 97-2; 1-2, 2-2	SS316L; 12-2	XM19; 12-3, 13-3	SS316L(N); 12-4	A286; 13-2	SS316L(N); 13-4	316L; 14-2	Inconel; 14-3	SS316L(N); 14-4	SS316L(N)-IG; 1-4
Mn	2.000×10^{-2}	1.880×10^{-2}	1.730×10^{-2}	1.800×10^{-3}	—	2.000×10^{-2}	1.500×10^{-2}	—	2.000×10^{-2}	1.520×10^{-2}
Fe	4.914×10^{-1}	6.565×10^{-1}	6.501×10^{-1}	4.260×10^{-2}	—	6.156×10^{-1}	5.317×10^{-1}	2.000×10^{-6}	6.156×10^{-1}	7.130×10^{-1}
Co	—	5.000×10^{-4}	2.000×10^{-4}	1.000×10^{-5}	5.000×10^{-4}	1.000×10^{-3}	4.000×10^{-4}	—	1.000×10^{-3}	—
Ni	2.700×10^{-1}	1.215×10^{-1}	1.250×10^{-1}	4.960×10^{-2}	—	1.400×10^{-1}	2.540×10^{-1}	5.000×10^{-5}	1.400×10^{-1}	8.120×10^{-2}
Cu	—	2.310×10^{-3}	7.000×10^{-4}	8.183×10^{-1}	9.879×10^{-1}	—	3.000×10^{-4}	—	—	—
Zn	—	—	—	1.600×10^{-4}	—	—	—	—	—	—
As	—	—	—	—	—	—	—	—	—	—
Zr	—	—	—	—	1.500×10^{-3}	—	—	—	—	—
Nb	—	1.600×10^{-4}	8.000×10^{-5}	1.000×10^{-5}	1.000×10^{-3}	5.000×10^{-4}	—	—	5.000×10^{-4}	—
Mo	1.500×10^{-2}	2.430×10^{-2}	2.340×10^{-2}	—	—	3.000×10^{-2}	1.240×10^{-2}	—	3.000×10^{-2}	—
Cd	—	—	—	1.000×10^{-5}	—	—	—	—	—	—
Sn	—	—	—	1.000×10^{-4}	—	—	—	—	—	—
Sb	—	—	—	—	—	—	—	—	—	—
Ta	—	8.000×10^{-5}	3.100×10^{-5}	1.000×10^{-5}	1.000×10^{-4}	—	—	—	—	—
W	—	—	—	—	—	—	—	9.997×10^{-1}	—	—
Pb	—	—	—	1.000×10^{-5}	—	—	1.000×10^{-6}	—	—	—

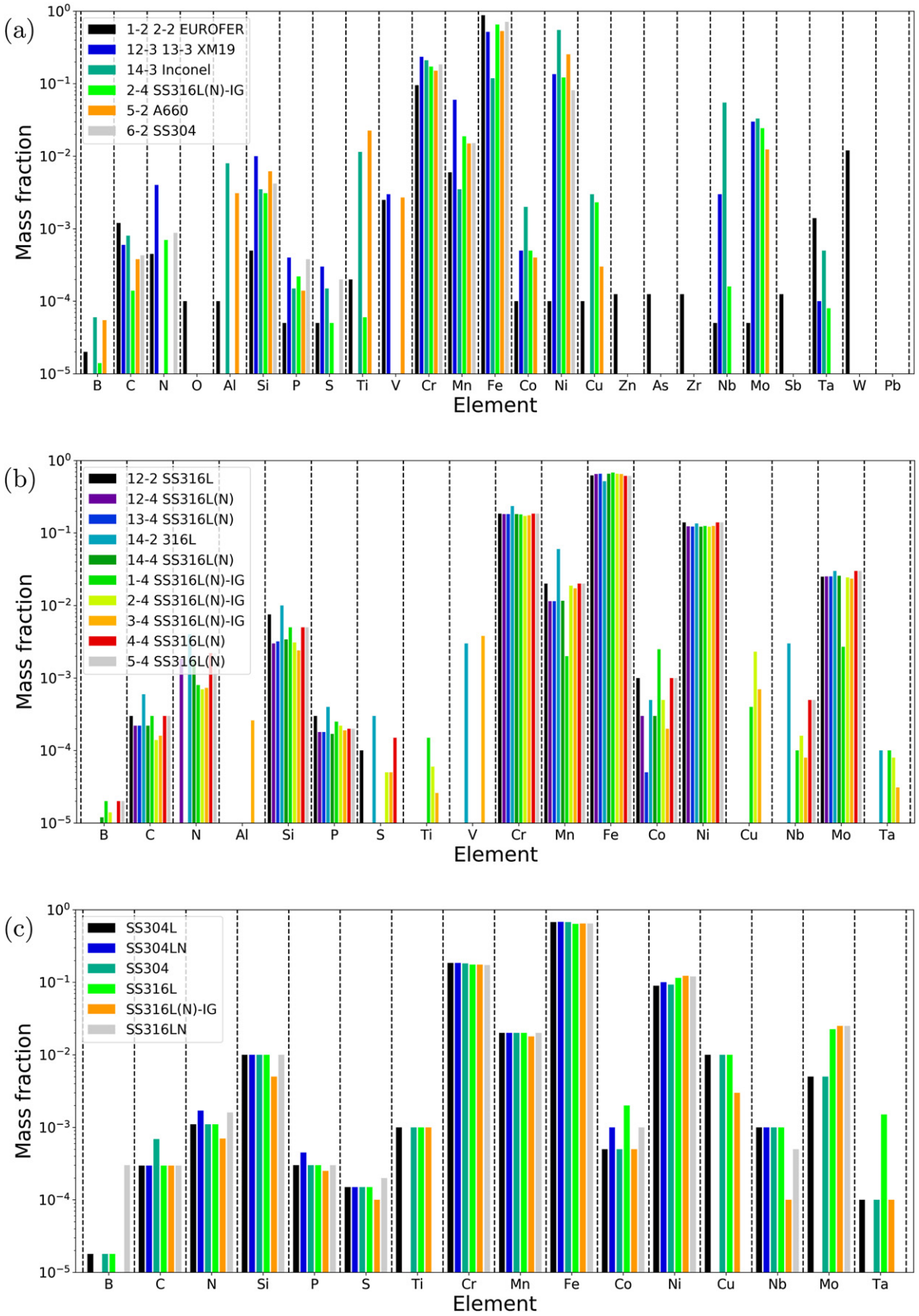

Figure 2. (*a*) Comparison of the elemental composition of various ITER steels as defined by the associated certificates. LTIS position IDs are provided in the legend and may be used with table 1 for fuller details; (*b*) comparison of the elemental composition of 316L alloy steels from different manufacturers (or batches) as defined in the associated certificates; (*c*) comparison of the elemental composition of selected steels as defined within the ITER materials activation handbook [16] and from [17].

mass, identified nuclide, decay corrected activity to the end of the JET irradiation period (20th December 2019 at 21:30:00 GMT), and measurement uncertainty. The methodology for calibration, analysis and reporting of activity results, which are detailed in the following paragraphs, were similar across each of the laboratories though some differences were noted, and there were also some difference in the HPGe instrument specifications themselves.

4.1. Instruments, calibration and analysis methodologies adopted across participating laboratories

Each of the participating laboratories used high resolution gamma spectrometry instruments to record sample gamma emission spectra. Various instruments with different specifications were used across these laboratories: CCFE used a broad energy germanium (BEGe) detector with a full width at half maximum (FWHM) energy-resolution of 1.69 keV at 1332 keV and relative efficiency of 26%, which was manufactured by MIRION (BEGe3825 SN 13135) and was contained within a low background graded lead shield. It was supplied with a LabSOCS characterisation file for the GENIE 2000 software. IFJ-PAN used coaxial detectors with 11% relative efficiency and planar HPGe detectors with Silena SpA electronics. The first detector was shielded by 100 mm of Pb, 2 mm of Cd and 20 mm of Cu, whereas the second detector had a passive shield with a 50 mm layer of Pb, 3 mm of Cu and 4 mm of acrylic glass. NCSRD used a coaxial detector (GEM80) with 85% relative efficiency, FWHM energy resolution of 1.67 keV at 1332 keV and a peak-to-Compton ratio of 93:1. ENEA used a 60% relative efficiency coaxial high purity Ge detector. IPPLM used a HPGe detector with resolution of 1.85 keV for 1332.4 keV gamma-ray of Co and 30% relative efficiency supplied with LabSOCS characterisation file.

Detector energy and efficiency calibration were performed using mixed radionuclide calibration sources or using LabSOCS software that has been traceably validated. Sealed mixed gamma sources typically including the following nuclides: ^{241}Am, ^{109}Cd, ^{57}Co, ^{51}Cr, ^{85}Sr, ^{54}Mn, ^{133}Ba, ^{137}Cs, ^{203}Hg, ^{60}Co and ^{88}Y were used. Sources have been traceably calibrated to a primary standard. The IFJ laboratory prepared specific sources from a mixed radionuclide solution containing ^{241}Am, ^{133}Ba, ^{137}Cs, ^{54}Mn and ^{60}Co, using standard solutions with known activity provided by the Czech Metrology Institute. The preparation process involved an accurately measured quantity of the mixed radionuclide solution pipetted onto a disc of filter paper placed on a thin metal layer (shim) with relevant composition and dimensions to the sample to be measured and analysed. After slow evaporation, the sources were hermetically sealed in PVC capsules using trichloroethylene.

In all laboratory cases the efficiency determination was performed at the relevant distance to which the ITER samples were measured: NCSRD samples were measured at source-to-detector distance of 1 cm; CCFE and IFJ-PAN at 0 cm (on the end cap) and ENEA at 10 cm distance.

A standard methodology for analysis was then followed: the activity at the end of the irradiation period, A_0, was determined experimentally via

$$A_0 = \frac{CG_\gamma}{t_c \epsilon_\gamma f_\gamma f_{TCC} e^{-\lambda t_d}}, \quad (1)$$

where C is the net counts acquired in the peak of interest during the counting time;

t_c is the counting time;

t_d is the time elapsed between the end of the irradiation and the start of the counting;

λ is the decay constant for the product radionuclide;

ϵ_γ is the full energy peak efficiency for the gamma-ray energy of interest;

f_γ is the number of gamma emissions of the energy of interest per disintegration;

G_γ is the gamma self-attenuation correction factor for the sample;

f_{TCC} is the true coincidence summing correction factor for the gamma emission.

C was determined from the detector acquired pulse height spectrum for a relevant gamma full energy peak region of interest by subtracting the background counts from the gross counts. This was done using commercially available software such as GammaVision or Genie2k in the case of ENEA, NCSRD, CCFE and IPPLM and via the in-house PIMP software developed at IFJ-PAN [18]. Correction factors to account for the gamma self-attenuation in the sample was either determined using MCNP or via LabSOCS. True coincidence summing factors were determined either via TrueCoic [19] or via LabSOCS [20].

4.2. Gamma spectrometry results

The tabulated decay corrected specific activity measurements covering all of the samples analysed in this work from all of the participating laboratories are provided in table 3. A selection of the raw gamma energy spectra obtained from CCFE sample measurements are highlighted in figure 3 which illustrate the characteristic peaks that are evident in these spectra ultimately used to quantify the activity of isotopes that are present. Figure 3(*a*) shows a spectrum obtained from an irradiated Inconel alloy 718 sample (LTIS position ID 14-3) acquired with a live time of 274648.2 s (approx. 3.2 days). One can observe the characteristic lines from ^{60}Co, ^{58}Co, ^{54}Mn, ^{51}Cr, ^{59}Fe, ^{65}Zn and ^{124}Sb in the Inconel-718 sample, which also shows evidence of ^{182}Ta being present, likely to originate from the presence of trace elemental Ta in the sample (reported in the certificate as Nb + Ta between 4.75 and 5.5 wt.% and Ta with max. 0.05 wt%). Also evident in the spectra is the true coincidence summation peak at around 1321 keV induced by an annihilation photon combined with the 810.5 keV ^{58}Co gamma line and the ^{60}Co sum peak around 2505 keV. The second example (figure 3(*b*)) is from an irradiated EUROFER 97-2 sample (LTIS position ID 1-2) acquired with a live time of 331857.7 s (approx. 3.8 d). One can observe the characteristic lines from ^{60}Co, ^{54}Mn, ^{65}Zn, ^{182}Ta, ^{185}W and ^{124}Sb. The non-labelled peaks that are evident in the spectra are the annihilation peak at 511 keV, characteristic x-rays from the Pb shield and numerous sum peaks mostly originating from

Table 3. Summary table of the gamma spectrometry results from all laboratories. Measured specific activities for the nuclides listed have been decay corrected to 20th December 2019 at 21:30:00 with uncertainties reported at 2 sigma. Minimum detectable activity values, where explicitly stated, were determined using the Currie limit. Samples 13-2, 4-3, and 13-4 were measured in an inter-laboratory comparison by IFJ-PAN and IPPLM and have been denoted by subscripts 1 and 2 respectively.

		Nuclide activity (Bq g^{-1})								
Sample pos. ID	Material	Co-58	Co-57	Co-60	Mn-54	Fe-59	Cr-51	Zn-65	Ta-182	Sb-124
1-2	EUROFER 97-2	<1.11	$<4.28 \times 10^{-2}$	$1.69 \times 10^{-1} \pm 2 \times 10^{-2}$	$2.08 \times 10^{1} \pm 2$	$<1.01 \times 10^{1}$	<8.74	$4.89 \times 10^{-1} \pm 9 \times 10^{-2}$	$2.24 \times 10^{2} \pm 9$	$3.39 \times 10^{1} \pm 2 \times 10^{1}$
3-2	Al-bronze	$5.85 \times 10^{1} \pm 6$	$1.46 \pm 2 \times 10^{-1}$	$3.20 \times 10^{-1} \pm \times 10^{-2}$	$1.13 \pm 1 \times 10^{-1}$	<1.09	$<2.99 \times 10^{1}$	$3.94 \times 10^{-1} \pm 5 \times 10^{-2}$	$2.97 \times 10^{-2} \pm 2 \times 10^{-2}$	$<3.48 \times 10^{-1}$
5-3	Tungsten	$<1.20 \times 10^{-1}$	$<3.03 \times 10^{-2}$	$8.30 \times 10^{-3} \pm 7 \times 10^{-3}$	$<1.26 \times 10^{-2}$	<1.06	$<3.96 \times 10^{1}$	$1.58 \times 10^{-1} \pm 4 \times 10^{-2}$	$<2.78 \times 10^{-1}$	$<2.12 \times 10^{-1}$
5-2	A660 alloy	$1.53 \times 10^{2} \pm 2 \times 10^{1}$	$3.87 \pm 6 \times 10^{-1}$	$1.44 \pm 9 \times 10^{-2}$	$1.68 \times 10^{1} \pm 2$	$4.20 \pm 7 \times 10^{-1}$	$1.52 \times 10^{2} \pm 5 \times 10^{1}$	$5.64 \times 10^{-1} \pm 7 \times 10^{-2}$	$<7.52 \times 10^{-2}$	$<4.85 \times 10^{-1}$
6-4	316L(N)	$1.42 \times 10^{2} \pm 2 \times 10^{1}$	$3.48 \pm 5 \times 10^{-1}$	$1.26 \pm 8 \times 10^{-2}$	$1.55 \times 10^{1} \pm 2$	$4.20 \pm 8 \times 10^{-1}$	$1.95 \times 10^{2} \pm 3 \times 10^{1}$	$5.44 \times 10^{-1} \pm 6 \times 10^{-2}$	$<7.65 \times 10^{-2}$	$2.09 \times 10^{-1} \pm 1 \times 10^{-1}$
12-4	316L(N)	$1.42 \times 10^{2} \pm 2 \times 10^{1}$	$3.57 \pm 5 \times 10^{-1}$	$1.49 \pm 1 \times 10^{-1}$	$1.58 \times 10^{1} \pm 2E{+}00$	$4.45 \pm 5 \times 10^{-1}$	$1.83 \times 10^{2} \pm 3 \times 10^{1}$	$4.14 \times 10^{-1} \pm 7 \times 10^{-2}$	$<4.17 \times 10^{-2}$	$1.77 \times 10^{-1} \pm 1 \times 10^{-1}$
12-3	XM19	$1.36 \times 10^{2} \pm 1 \times 10^{1}$	$3.37 \pm 5 \times 10^{-1}$	$1.43 \pm 9 \times 10^{-2}$	$1.59 \times 10^{1} \pm 2E{+}00$	$3.71 \pm 4 \times 10^{-1}$	$2.14 \times 10^{2} \pm 4 \times 10^{1}$	$4.72 \times 10^{-1} \pm 5 \times 10^{-2}$	$1.67 \pm 1 \times 10^{-1}$	$2.38 \times 10^{-1} \pm 1 \times 10^{-1}$
12-2	316L	$1.45 \times 10^{2} \pm 2 \times 10^{1}$	$3.63 \pm 5 \times 10^{-1}$	$1.47 \pm 1 \times 10^{-1}$	$1.66 \times 10^{1} \pm 2E{+}00$	$4.71 \pm 4 \times 10^{-1}$	$1.67 \times 10^{2} \pm 3 \times 10^{1}$	$5.06 \times 10^{-1} \pm 5 \times 10^{-2}$	$1.08 \times 10^{-1} \pm 2 \times 10^{-2}$	$<5.74 \times 10^{-2}$
14-3	Inconel	$6.44 \times 10^{2} \pm 7 \times 10^{1}$	$1.61 \times 10^{1} \pm 2$	$2.61 \pm 2 \times 10^{-1}$	$4.51E{+}00 \pm 5 \times 10^{-1}$	$1.40 \pm 1 \times 10^{-1}$	$1.63 \times 10^{2} \pm 3 \times 10^{1}$	$4.83 \times 10^{-1} \pm 6 \times 10^{-2}$	$1.08 \times 10^{1} \pm 5 \times 10^{-1}$	$<1.15 \times 10^{-1}$
14-2	316L	$1.48 \times 10^{2} \pm 2 \times 10^{1}$	$3.68 \pm 5 \times 10^{-1}$	$1.48 \pm 1 \times 10^{-1}$	$1.69 \times 10^{1} \pm 2E{+}00$	$4.64 \pm 4 \times 10^{-1}$	$1.59 \times 10^{2} \pm 3 \times 10^{1}$	$5.16 \times 10^{-1} \pm 6 \times 10^{-2}$	$1.95 \times 10^{-1} \pm 3 \times 10^{-2}$	$<1.19 \times 10^{-1}$
3-4	316L(N)-IG	$1.45 \times 10^{2} \pm 2 \times 10^{1}$	$3.60 \pm 5 \times 10^{-1}$	$2.39 \pm 2 \times 10^{-1}$	$1.65 \times 10^{1} \pm 2E{+}00$	$4.65 \pm 4 \times 10^{-1}$	$1.66 \times 10^{2} \pm 3 \times 10^{1}$	$5.33 \times 10^{-1} \pm 1 \times 10^{-1}$	$1.52 \times 10^{-1} \pm 3 \times 10^{-2}$	$<2.05 \times 10^{-1}$
1-4	316L(N)-IG	$1.97 \times 10^{2} \pm 6$	$4.20 \pm 4 \times 10^{-1}$	$1.90 \pm 2 \times 10^{-1}$	$2.00 \times 10^{1} \pm 7 \times 10^{-1}$	—	—	—	—	—
4-4	316L(N)	$1.92 \times 10^{2} \pm 6$	$4.30 \pm 5 \times 10^{-1}$	$1.00 \pm 3 \times 10^{-1}$	$2.04 \times 10^{1} \pm 8 \times 10^{-1}$	—	—	—	—	—
14-4	316L(N)	$2.01 \times 10^{2} \pm 7$	$3.90 \pm 6 \times 10^{-1}$	$1.70 \pm 6 \times 10^{-1}$	$2.15 \times 10^{1} \pm 9 \times 10^{-1}$	—	—	—	—	—
1-3	A660 alloy	$3.91 \times 10^{2} \pm 1 \times 10^{1}$	$1.80 \times 10^{1} \pm 1E{+}00$	$7.50 \pm 2 \times 10^{-1}$	$1.78 \times 10^{1} \pm 7 \times 10^{-1}$	—	—	—	—	—
6-3	Tungsten	—	—	—	—	—	—	—	—	—
13-3	XM19	$1.90 \times 10^{2} \pm 6$	$4.10 \pm 4 \times 10^{-1}$	$1.80 \pm 3 \times 10^{-1}$	$2.06 \times 10^{1} \pm 7 \times 10^{-1}$	—	—	—	—	—
2-2	EUROFER 97-2	—	—	—	$2.65 \times 10^{1} \pm 1E{+}00$	$3.53 \times 10^{1} \pm 1 \times 10^{1}$	—	—	$2.40 \times 10^{2} \pm 1 \times 10^{1}$	—
6-2	SS304	$1.93 \times 10^{2} \pm 6$	$4.70 \pm 9 \times 10^{-1}$	$1.70 \pm 4 \times 10^{-1}$	$2.03 \times 10^{1} \pm 8 \times 10^{-1}$	—	—	—	—	—
$13\text{-}2_1$	A286 alloy	$2.99 \times 10^{2} \pm 3 \times 10^{1}$	$8.37 \pm 9 \times 10^{-1}$	$1.02 \pm 5 \times 10^{-2}$	$1.52 \times 10^{1} \pm 2E{+}00$	$3.92 \pm 7 \times 10^{-1}$	$1.87 \times 10^{2} \pm 2 \times 10^{1}$	$4.79 \times 10^{-1} \pm 9E{-}02$	—	—
$4\text{-}3_1$	CuCrZr	—	—	$3.34 \times 10^{-1} \pm 3 \times 10^{-2}$	—	—	9.70 ± 2	$2.66 \times 10^{-1} \pm 6 \times 10^{-2}$	—	—
$13\text{-}4_1$	316L(N)	$1.46 \times 10^{2} \pm 1 \times 10^{1}$	$4.09 \pm 4 \times 10^{-1}$	$1.48 \pm 6 \times 10^{-2}$	$1.55 \times 10^{1} \pm 2E{+}00$	$5.81 \pm 9 \times 10^{-1}$	$2.21 \times 10^{2} \pm 3 \times 10^{1}$	—	—	—
$13\text{-}2_2$	A286 alloy	$3.26 \times 10^{2} \pm 2 \times 10^{1}$	$8.24 \pm 8 \times 10^{-1}$	$9.50 \times 10^{-1} \pm 6 \times 10^{-2}$	$1.68 \times 10^{1} \pm 1E{+}00$	—	—	$5.20 \times 10^{-1} \pm 6 \times 10^{-2}$	—	—
$4\text{-}3_2$	CuCrZr	—	—	$2.80 \times 10^{-1} \pm 2 \times 10^{-2}$	—	—	—	$2.00 \times 10^{-1} \pm 2 \times 10^{-2}$	—	—
$13\text{-}4_2$	316L(N)	$1.56 \times 10^{2} \pm 8$	$3.92 \pm 4 \times 10^{-1}$	$1.37 \pm 9 \times 10^{-2}$	$1.60 \times 10^{1} \pm 2E{+}00$	$5.07 \pm 7 \times 10^{-1}$	—	—	—	—
4-2	Al−bronze	$8.87 \times 10^{1} \pm 1 \times 10^{1}$	$1.84E{+}00 \pm 3 \times 10^{-1}$	$6.63 \times 10^{-1} \pm 8 \times 10^{-2}$	$1.69E{+}00 \pm 2 \times 10^{-1}$	$6.69 \times 10^{-1} \pm 4 \times 10^{-1}$	—	$9.60 \times 10^{-1} \pm 1 \times 10^{-1}$	—	—
5-4	316L(N)	$2.32 \times 10^{2} \pm 3 \times 10^{1}$	$4.93 \pm 6 \times 10^{-1}$	$2.15 \pm 3 \times 10^{-1}$	$2.45 \times 10^{1} \pm 3E{+}00$	$6.35 \pm 8 \times 10^{-1}$	$2.48 \times 10^{2} \pm 3 \times 10^{1}$	$6.49 \times 10^{-1} \pm 9 \times 10^{-2}$	—	$5.18 \times 10^{-1} \pm 2 \times 10^{-1}$
2-4	316L(N)-IG	$2.07 \times 10^{2} \pm 2 \times 10^{1}$	$4.48 \pm 6 \times 10^{-1}$	$1.77 \pm 2 \times 10^{-1}$	$2.25 \times 10^{1} \pm 3E{+}00$	$6.67 \pm 9 \times 10^{-1}$	$2.54 \times 10^{2} \pm 3 \times 10^{1}$	$1.14 \pm 2 \times 10^{-1}$	—	—

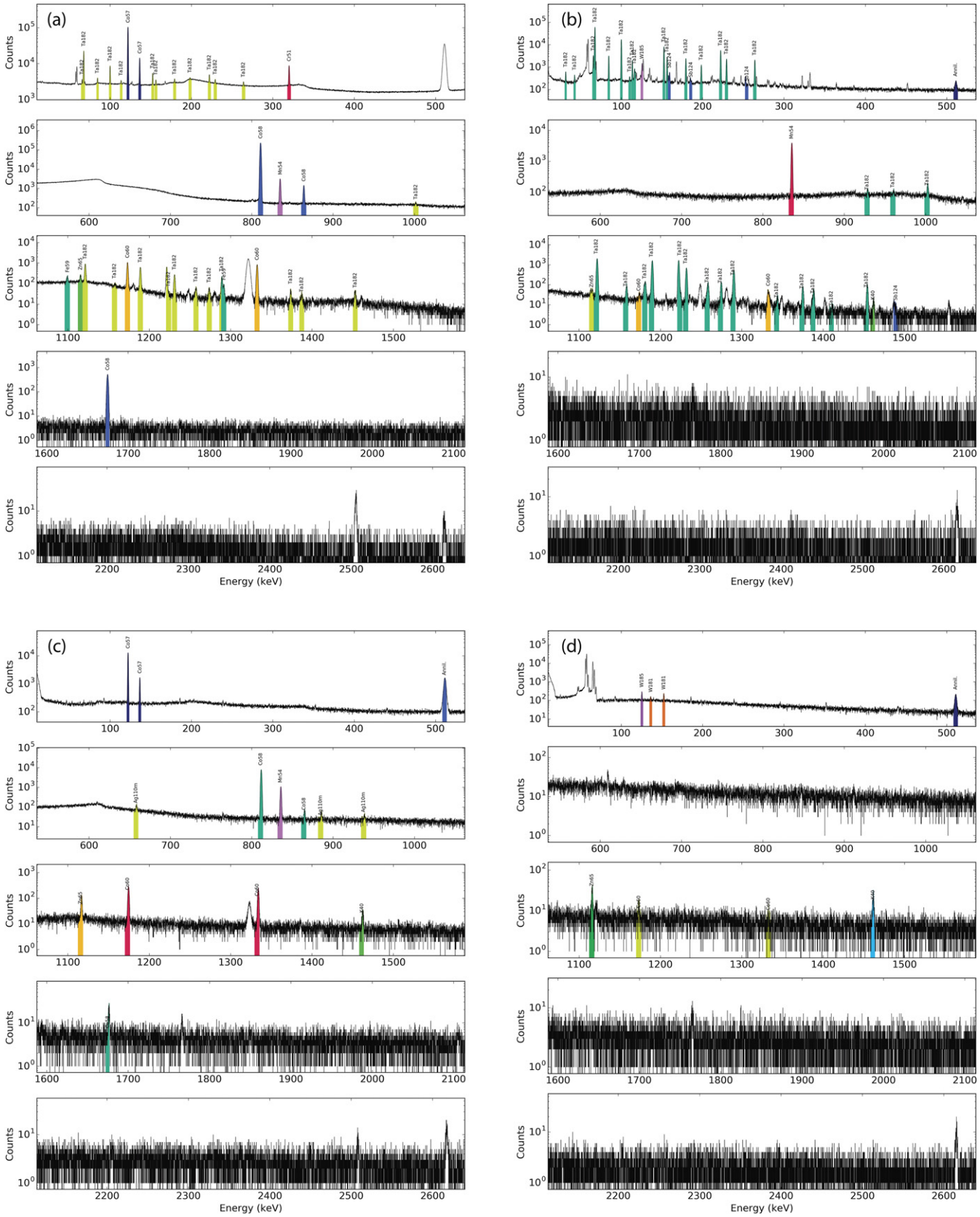

Figure 3. HPGe measurement taken from: (*a*) Inconel sample position ID: 14-3; (*b*) EUROFER 97-2 sample position ID: 1-2; (*c*) Al–Bronze alloy, position ID: 3-2; (*d*) W divertor monoblock, position ID: 5-3.

^{182}Ta. The sample shows evidence of comparatively high ^{182}Ta compared to other steels, which is expected since the element is present in EUROFER 97-2 by design (see table 2). The ^{182}Ta specific activity measurements for two EUROFER 97-2 samples at ENEA and CCFE, which were 240 $\pm$ 10 and 224 $\pm$ 9 Bq g^{-1}, respectively, are consistent with each other. Whilst ^{182}Ta presents a significant contribution to the overall gamma dose from EUROFER 97-2, on shorter timescales (of the order of 1 year cooling), when compared to several other elements such as Ni, Cu, Zr, Nb and Mo, the long-term activation products from Ta in general is more favourable from a waste disposal perspective when compared to several other elements. The time needed to reach the UK low level waste (LLW) criteria for Ta is only 41 y compared to >1000 y needed for the above mentioned elements. Figure 9in [21] which provides an elemental assessment for the full periodic table of the time duration for waste to meet identified LLW criteria after being exposed to fusion irradiation conditions. Figures 3(*c*) and (*d*) show spectra obtained from Al–bronze alloy and divertor monoblock spectra respectively.

5. Calculated post-irradiation specific activities using FISPACT-II and MCNP

Activation calculations have been conducted using the FISPACT-II inventory code [13] for the JET operational period in order to predict the dosimetry foil activities as a function of time. This was performed using a detailed JET model (referred to as the 'UU model') within the MCNPv6.2 [22] code using the FENDL-3.1b [23] radiation transport library to calculate the neutron spectrum at the specific material cell position within the LTIS. The MCNP model that was developed included a detailed representation of the LTIS and ACT subholder. The model geometry and material specification was prepared with the exact loading arrangement used in the experiment. The simulations were performed with 1 $\times$ 10^9 neutron histories with coupled neutron–gamma mode, both for a D–D plasma neutron source and also for a D–T plasma neutron source. The AutomateD VAriaNce reducTion Generator (ADVANTG) software [24] was used to generate a target optimised weight window map subsequently applied to the production calculation in order to reduce the neutron flux tally variance at the LTIS position. All volumetric neutron flux (F4 tally) results passed the 10 statistical tests and the simulation was deemed to have converged satisfactorily. JSI performed analysis on the dosimetry foil measurements based on a combined DD/DT neutron energy spectrum for the C38 deuterium campaign. The activities due to reactions with energy thresholds higher than 4 MeV are compatible with 1.4% plasma source D–T neutrons with the remainder attributed to DD plasma neutrons. The inset neutron spectrum, shown in figure 4, exhibits the two characteristic neutron energy peaks from the D–D and D–T fusion reactions. Although the principal operation mode of JET was in D–D plasma mode in this campaign, resulting in the production of neutrons around 2.45 MeV, the triton produced from one branch of this reaction leads to 14 MeV neutrons being present in the field through subsequent D–T reactions [25, 26]. For the FISPACT-II inventory calculations MCNP-derived pointwise spectrum-averaged cross sections were used as input for all dosimetry reaction channels; IRDFF-II [27] pointwise data were used where possible, JEFF 3.3 pointwise data were used otherwise. The EAF-2010 group-wise activation library in 175 energy groups was used for all other reaction channels not covered by these two libraries.

The irradiation history used as an input to perform inventory simulations was derived from total neutron yield measurement data. The LTIS containing the samples was installed on the 27th July 2019 and retrieved on 20th December 2019 at 9.30 pm, and was exposed to JET neutrons over a 147 day period. During the portion of the C38 campaign that the LTIS was installed in JET a total neutron yield of 3.151 $\times$ 10^{19} was measured using the JET fission chamber diagnostic system, also referred to as the KN1 system. KN1 consists of three pairs of ^{235}U and ^{238}U fission chambers. The chambers are mounted on the vertical magnetic limbs located in octants 2, 6, and 8, at a radius of 782 cm in the equatorial plane at the JET facility. Further details in relation to the KN1 diagnostic system are described in [11, 28]. The neutron fluence temporal profile was modeled with 1 week time resolution using flat top pulses, calculated using the KN1 daily measured neutron yield multiplied by the appropriate MCNP flux normalisation for the relevant sample position within the LTIS. This data was then used as the temporal irradiation history input to the subsequent FISPACT-II calculations. Figure 4 shows an example of the JET irradiation history (here the data is shown in 1 day time resolution) and predicted specific activity results for various dominant nuclides obtained from these activation calculations for an EUROFER 97-2 steel sample.

6. Discussion and comparison of experimental against calculation results

FISPACT-II calculation predictions (*C*) at the end of the JET irradiation were compared against experimental data (*E*), the decay corrected specific activity measurement results, to produce *C*/*E* results. The summarised results are shown as combined weighted average dosimetry foil *C*/*E* values per reaction in figure 5 and for individual ITER materials in figures 6(*a*) and (*b*).

For the dosimetry foil measurements some general comments relating to the threshold reactions, sensitive to the fast neutron spectrum, can be made. The reactions in figure 5 show two capture reactions, ^{59}Co(n, γ)^{60}Co and ^{45}Sc(n, γ)^{46}Sc, and seven threshold reactions (ascending in threshold energy from left to right). Weighted average *C*/*E* per reaction type have been calculated using the inverse variance method applied to the relevant data sets. Whilst figure 5 shows that the ^{60}Ni(n, p)^{60}Co, ^{nat}Ti(n, x)^{46}Sc and ^{58}Ni(n, $n'p$)^{57}Co reactions exhibit slightly high *C*/*E* values, the KN1 measurement uncertainty is reported as 10%. As discussed in more detail in [15] the most significant difference between calculations and measurements is observed for the Co and Sc sample capture measured by IFJ appear to be systematically high by up to around 30%. Only one measurement for the ^{nat}Ti(n, x)^{46}Sc reaction was

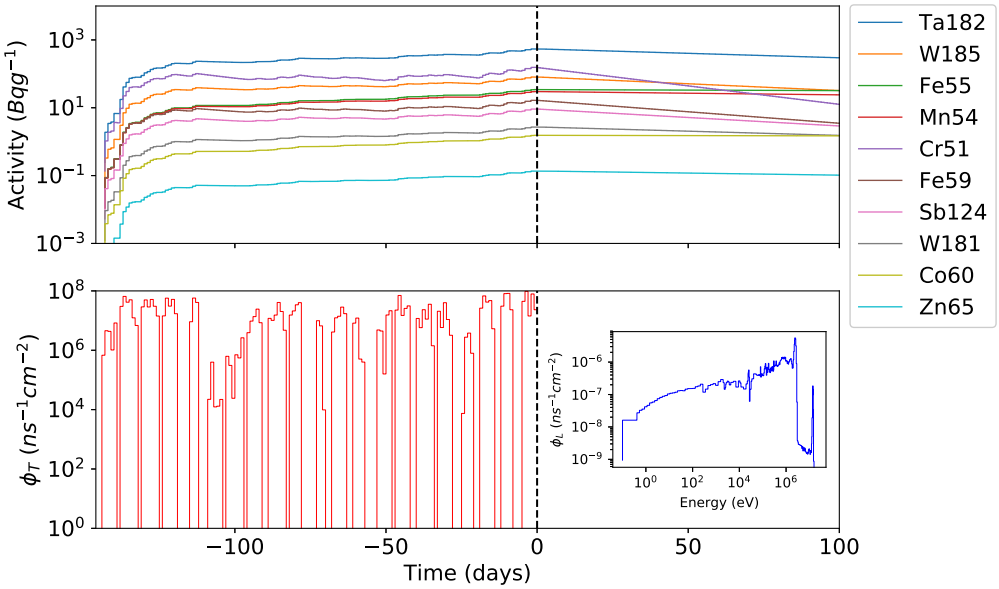

Figure 4. (Top plot) Specific activity prediction of dominant nuclides during and following JET irradiation of an EUROFER 97-2 sample (position reference 1-2). The dashed vertical line denotes the time at which the samples were removed from the JET LTIS. (Bottom plot) Daily neutron fluence averaged over the sample volume within the LTIS, ϕ_{T}. The inset plot shows the neutron fluence per unit lethargy, ϕ_{L}, energy spectrum averaged over the sample volume within the LTIS, calculated using MCNP.

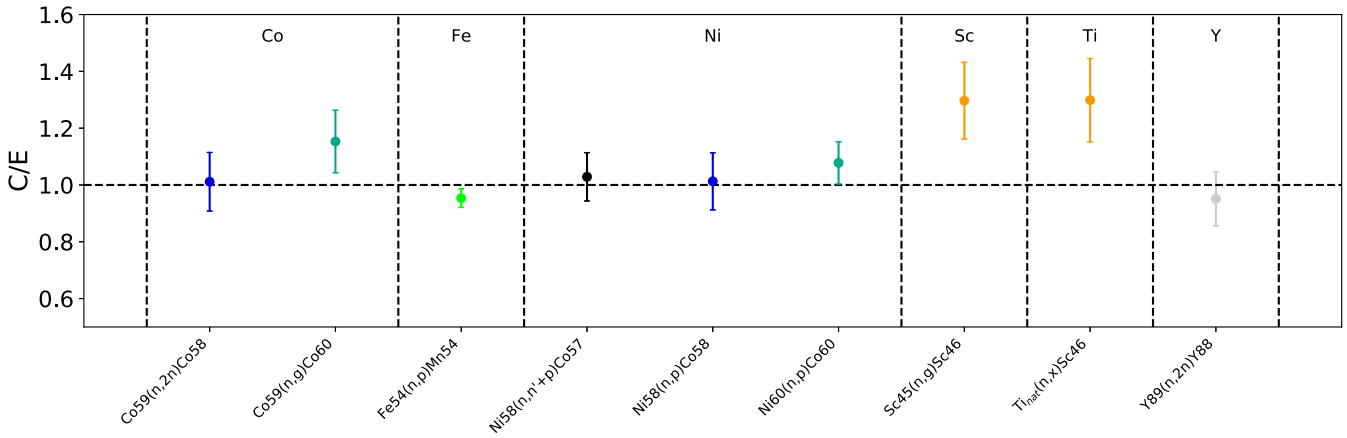

Figure 5. Weighted average *C*/*E* values for sets of dosimetry foil reactions. Experimental uncertainties are reported at 1 sigma.

available though is also high at 1.3. Aside from these variations the data results show that the calculated neutron fluence for the fast neutron spectrum and lower energy neutron region is largely consistent with experimental observation. A D–T triton burnup fraction of 1.4% has been assumed here, discussed in more detail in [15]. For comparison with this value typical values of the D–T fraction have been reported to be around 1% previously [25, 26] during previous JET deuterium plasma operations.

For the ITER materials the full data set shown in figure 6. These present: in (*a*) the *C*/*E* values per measured isotope with measurement laboratories identified; and in (*b*) the same *C*/*E* data set, but grouped by the material type. In general it can be seen that the isotope measurements for ^{57}Co, ^{58}Co, ^{51}Cr, ^{59}Fe and ^{54}Mn are closest to 1 with averaged *C*/*E* values of 1.2, 1.37, 1.39, 1.36 and 1.08 respectively per isotope. It is stressed that because the materials are complex compounds of different elemental compositions (as compared to high purity, elemental dosimetry foil materials) isotope measurement results may include different reaction pathways to the reaction product, for example ^{60}Co data may include reaction pathways from $^{59}\mathrm{Co}(n,\gamma)^{60}\mathrm{Co}$ and $^{60}\mathrm{Ni}(n,p)^{60}\mathrm{Co}$. A relatively greater spread is evident for ^{60}Co and the 26 data points presented tend to be above 1 apart from 4 data points with an average *C*/*E* value of 6.55 associated with a range of values extending from 0.004 to 29.

In the case of the 316L type steels, of which there were several samples from different manufacturers, the measured ^{60}Co activity ranges from 1.0 ± 0.3 Bq g^{-1} to 2.39 ± 0.2 Bq g^{-1} which were for sample IDs 4-4 and 3-4 respectively. Sample ID 4-4 was Thyssen Krupp Radial plates used for the ITER toroidal field coils with a (Schmiedewerke Gröditz) certificate reported heat analysis Co elemental mass fraction of 2.0×10^{-4} and a maximum of 1.0×10^{-3} and a heat analysis

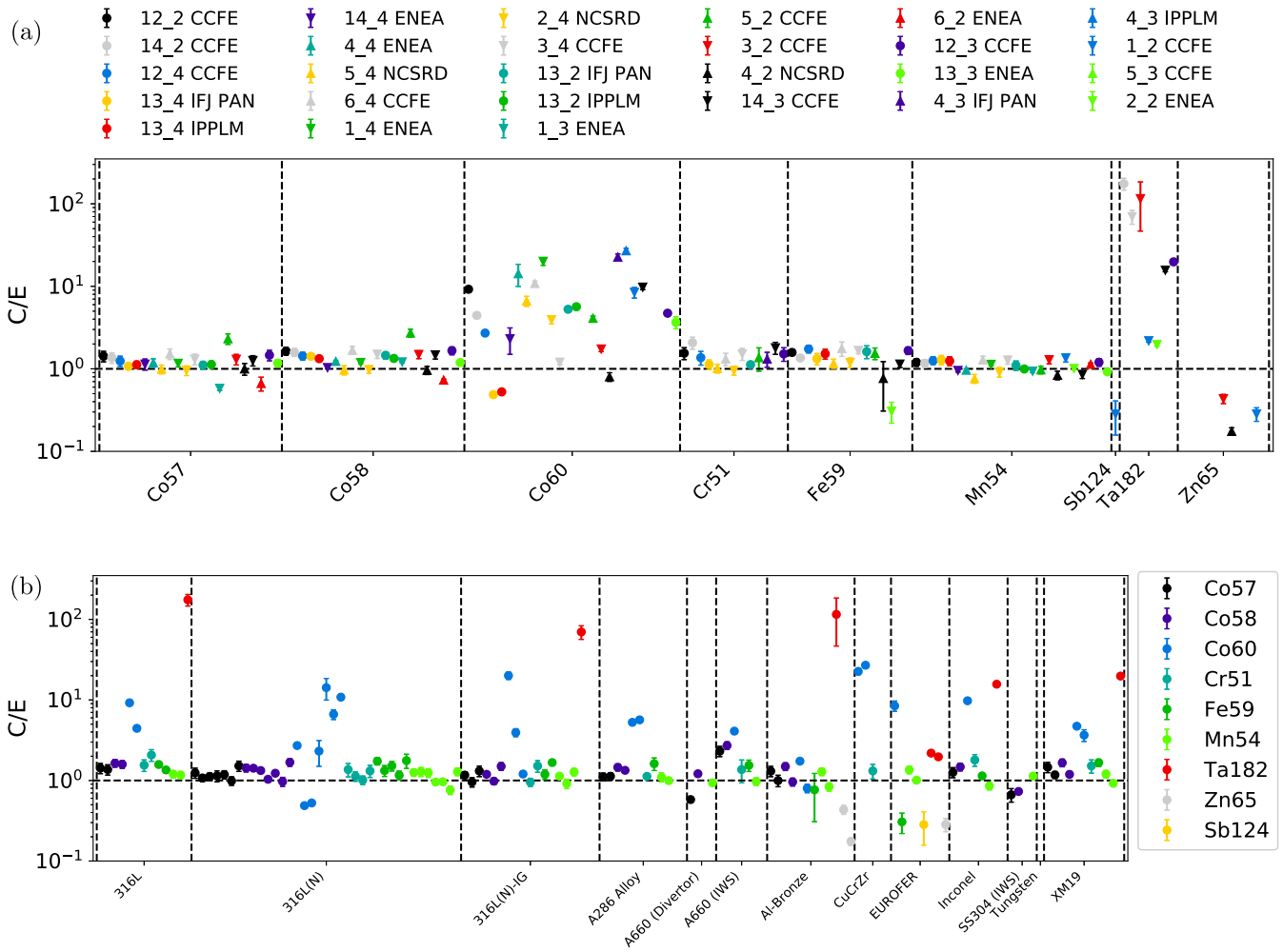

Figure 6. *C/E* values for measured and calculated ITER materials: (*a*) results grouped by measured isotope (isotope measurement results may be from different reaction pathways). The legend indicates the position–depth ID linked to the material description in table 1 and the measurement laboratory; (*b*) results grouped by material type.

Ni elemental mass fraction of 1.23×10^{-1} with maximum 1.4×10^{-1}. Sample ID 3-4 was Thyssen Krupp ITER grade vacuum vessel plate with a (Schmiedewerke Gröditz) certificate reported Co elemental mass fraction 2.0×10^{-4} and Ni elemental mass fraction 1.25×10^{-1} (the latter sample certificate specified no minimum or maximum element mass range). Sample ID 4-4 showed a significantly higher *C/E* result of 14 $\pm$ 30% i.e. lower measured ^{60}Co than expected from the calculations. Since the primary routes to the production of ^{60}Co in the JET neutron environment is via ^{59}Co(n, γ)^{60}Co and via ^{60}Ni(n, p)^{60}Co, a relative comparison of the measured activity results of these two samples appears to be inconsistent with the expected activities based on the certificated levels of Co and Ni content.

Two XM-19 steels that were measured at ENEA and CCFE show good agreement with each other for the reported nuclide activities. A separate intercomparison between IFL and IPPLM gamma spectrometry systems for A286 alloy, CuCrZr and a 316L(N) steel broadly showed that good agreement has been obtained between these laboratories, with the IPPLM/IFJ-PAN ratio being between 0.9 and 1.1 for most nuclides. Some activity values for short-lived nuclides evident in the CuCrZr and 316L(N) samples using IFJ-PAN measurements were not reported by IPPLM as the activity levels were below the limit of detection at the time of measurement several months later.

Two significantly low *C/E* values for ^{65}Zn have been observed from the EUROFER 97-2 and A660 alloy measurements. These results are not shown in figure 6 as the *C/E* results are in the region of 1×10^{-12}. The ^{124}Sb *C/E* value is also low for EUROFER 97-2 sample 1_2, at 0.28. Notable C/*E* deviations from 1 are also observed for some ^{182}Ta *C/E* results, a number of which were high, for example Al–Bronze, XM-19 and Inconel, with a particularly high *C/E* value of 175 for the divertor Nadege 316L steel (sample 14-2). These particular deviations require further investigation—one possibility is that the impurity levels in the samples may not be according to the material specification certificate.

7. Conclusions

The status of experimental activities at JET, focusing on the irradiation of real ITER materials and elemental dosimetry foils within the C38 deuterium campaign was presented.

27 ITER material samples were exposed to neutrons from the JET plasma with a neutron yield of 3.151×10^{19} in 2019. The samples were then retrieved and distributed to laboratories for analysis in early 2020. Gamma spectrometry using HPGe detectors and analysis were performed at five laboratories (CCFE, ENEA, NCSRD, IPPLM and IFJ-PAN). The analysis identified a number of activation products measured in each sample and corresponding modelling predictions have been compared against these observations.

The dosimetry foil measurements for most reactions show that the calculated neutron fluence for the fast neutron spectrum, including the D–T fraction due to triton burn-up, and lower energy neutron regions are close to the experimental observations. Some differences between calculations and measurements have however been observed for a small sub-set of data points for Co, Sc and Ti samples, which appear to be slightly higher by up to 30%.

For the ITER material results the full data set of *C*/*E* values per measured isotope has been presented briefly with some initial remarks in this short paper, though will be discussed in more detail in a more extensive future paper. The measurements for ^{57}Co, ^{58}Co, ^{51}Cr, ^{59}Fe and ^{54}Mn are observed to be closest to 1, with averaged values per nuclide within the range 1.08–1.39, indicating a slight overestimation of calculation predictions. A relatively greater spread in *C*/*E* results for ^{60}Co is evident with an average *C*/*E* of 6.55. Highlighted discrepancies in *C*/*E* values have been noted for ^{65}Zn, ^{124}Sb and ^{182}Ta which require further investigation.

Installation of the LTIS with new samples was completed in September 2020, in readiness for the combined irradiation of the LTIS during the C40 T–T experimental campaign in 2021 followed by the DTE2 (D–T) campaign. The samples included a range of ITER materials, dosimetry foils, VERDI detectors [29] and thin samples of W, Mo and Fe to study for radiation-induced defects. These samples are expected to be retrieved in 2022 and then measured either by low background HPGe gamma spectrometry techniques or, in the case of the thin W, Mo and Fe samples, measured by the PALS technique to determine the density and size distribution of radiation-induced defects.

Acknowledgments

This work has been carried out within the framework of the EUROfusion Consortium and has received funding from the Euratom Research and Training Programme 2014–2018 and 2019–2020 under Grant agreement No. 633053 and from the RCUK Energy Programme [Grant No. EP/T012250/1]. The views and opinions expressed herein do not necessarily reflect those of the European Commission.

ORCID iDs

M. Fabbri https://orcid.org/0000-0002-9979-3025
M.R. Gilbert https://orcid.org/0000-0001-8935-1744
M. Pillon https://orcid.org/0000-0001-5534-6859

References

[1] Joffrin E. *et al* 2019 Overview of the JET preparation for deuterium–tritium operation with the ITER like-wall *Nucl. Fusion* **59** 112021
[2] Batistoni P. 2016 On the absolute calibration of neutron measurements in fusion reactors *Fusion Eng. Des.* **105** 58–69
[3] Villari R. *et al* 2016 Neutronics experiments and analyses in preparation of DT operations at JET *Fusion Eng. Des.* **109–111** 895–905
[4] Villari R. *et al* 2017 ITER oriented neutronics benchmark experiments on neutron streaming and shutdown dose rate at JET *Fusion Eng. Des.* **123** 171–6
[5] Obryk B., Batistoni P., Conroy S., Syme B.D., Popovichev S., Stamatelatos I.E., Vasilopoulou T. and Bilski P. 2014 Thermoluminescence measurements of neutron streaming through JET Torus Hall ducts *Fusion Eng. Des.* **89** 2235–40
[6] Batistoni P., Conroy S., Lilley S., Naish J., Obryk B., Popovichev S., Stamatelatos I., Syme B. and Vasilopoulou T. 2015 Benchmark experiments on neutron streaming through JET Torus Hall penetrations *Nucl. Fusion* **55** 053028
[7] Vasilopoulou T., Stamatelatos I.E., Batistoni P., Conroy S., Obryk B., Popovichev S. and Syme D.B. 2015 Neutron streaming along ducts and labyrinths at the JET biological shielding: effect of concrete composition *Radiat. Phys. Chem.* **116** 359–64
[8] Colling B., Batistoni P., Bradnam S.C., Ghani Z., Gilbert M.R., Nobs C.R., Packer L.W., Pillon M. and Popovichev S. 2017 Testing of tritium breeder blanket activation foil spectrometer during JET operations *Fusion Eng. Des.* **136** 258–64
[9] Packer L.W. *et al* 2017 Status of ITER material activation experiments at JET *Fusion Eng. Des.* **124** 1150–5
[10] Stankunas G., Tidikas A., Batistoni P. and Lengar I. 2017 Analysis of activation and damage of ITER material samples expected from DD/DT campaign at JET *Fusion Eng. Des.* **125** 307–13
[11] Packer L.W. *et al* 2018 Activation of ITER materials in JET: nuclear characterisation experiments for the long-term irradiation station *Nucl. Fusion* **58** 096013
[12] Sublet J.-C, Eastwood J.W. and Morgan J.G. 2014 The FISPACT-II user manual *Technical Report CCFE-R(11) 11 Issue 6* CCFE
[13] Sublet J.-C., Eastwood J.W., Morgan J.G., Gilbert M.R., Fleming M. and Arter W. 2017 *Nucl. Data Sheets* **139** 77–137
[14] Pelowitz D.B. *et al* 2013 MCNP6 user's manual version 1 *Los Alamos Document Number: LA-CP-13-00634, Rev. 0*
[15] Zohar A. *et al* 2021 Long term neutron activation in JET DD operation *ANNIMA Conf. Proc.* (Prague, Czech Republic, 21–25 June 2021) (https://indico.utef.cvut.cz/event/23/)
[16] Gilbert M.R. *et al* 2016 Handbook of activation, transmutation, and radiation damage properties of the elements and of ITER materials simulated using FISPACT-II & TENDL-2015; ITER FW armour focus *Technical Report* (https://fispact.ukaea.uk/wp-content/uploads/2016/10/CCFE-R1637.pdf)
[17] Barabash V. 2016 Chemical compositions of materials representing the components included into basic model for nuclear analysis of ITER, ITER document series, ITER-D-HTN8X3 v 2.1 *Technical Report* (private communication)
[18] Mietelski J.W. 1989 *Technical Report*, Report IFJ PAN No. 1435/S (Kraków) (https://inis.iaea.org/collection/NCLCollectionStore/_Public/21/076/21076770.pdf) (private communication)
[19] Sudar S. 2017 A program for calculation of true coincidence corrections for gamma rays *TRUECOINC (Version 1.01a)* (Debrecen, Hungary: University of Debrecen) (http://kisfiz.

phys.klte.hu/kisfiz/sudar/TrueCoinc/TrueCoincUserGuide.pdf)
[20] ISOCS/LabSOCS 2021 Detector efficiency characterization *Technical Report* (https://mirion.com/products/labsocs-calibration-software)
[21] Gilbert M.R., Eade T., Rey T., Vale R., Bachmann C., Fischer U. and Taylor N.P. 2019 Waste implications from minor impurities in european DEMO materials *Nucl. Fusion* **59** 076015
[22] Werner J.C. *et al* 2018 *MCNP Version 6.2 Release Notes*
[23] IAEA 2021 Fusion evaluated nuclear data library-FENDL-3.2 (https://nds.iaea.org/fendl/)
[24] Mosher S.W. *et al* 2015 ADVANTG—an automated variance reduction parameter generator, ORNL/TM-2013/416 Rev. 1 *Technical Report* (Oak Ridge, TN: Oak Ridge National Laboratory)
[25] Conroy S., Jarvis O.N., Sadler G. and Huxtable G.B. 1988 Time resolved measurements of triton burnup in JET plasmas *Nucl. Fusion* **28** 2127
[26] Jarvis O.N. and Conroy S. 2002 Prediction/modelling of the neutron emission from JET discharges *Plasma Phys. Control. Fusion* **44** 1651
[27] Trkov A. *et al* 2020 IRDFF-II: a new neutron metrology library vol 163 1–108 (https://sciencedirect.com/science/article/pii/S0090375219300687)
[28] International Atomic Energy Agency 2020 Modern neutron detection, IAEA-TECDOC-1935, IAEA, Vienna; article: neutron detection and measurement challenges at JET and ITER *Technical Report* (https://iaea.org/publications/14690/modern-neutron-detection)
[29] Savva M.I. *et al* 2019 VERDI detector benchmark experiment at the ENEA 14 MeV Frascati Neutron Generator *Fusion Eng. Des.* **146** 1877–81